We are IntechOpen, the world's leading publisher of Open Access books Built by scientists, for scientists

4,800
Open access books available

122,000
International authors and editors

135M
Downloads

Our authors are among the

154
Countries delivered to

TOP 1%
most cited scientists

12.2%
Contributors from top 500 universities

WEB OF SCIENCE™

Selection of our books indexed in the Book Citation Index in Web of Science™ Core Collection (BKCI)

Interested in publishing with us?
Contact book.department@intechopen.com

Numbers displayed above are based on latest data collected.
For more information visit www.intechopen.com

14

Microstructure and High-Temperature Strength of 9CrODS Ferritic Steel

Shigeharu Ukai
Hokkaido University
Japan

1. Introduction

Oxide-dispersion-strengthened (ODS) ferritic steel is known to be candidates for advanced fission and fusion materials that require excellent radiation resistance and high-temperature capabilities (Odette et al., 2008). We focus on the development of 9CrODS ferritic steel with a composition of Fe-9Cr-0.13C-2W-0.2Ti-0.35Y_2O_3 (mass%) (Ohtsuka et al., 2004, 2005a, 2005b, 2006, 2007; Ukai et al., 1998, 2002a, 2002b, 2003, 2007, 2009, 2011; Yamamoto et al., 2010, 2011). This steel contains nano-size Y-Ti complex oxide particles. Its microstructures can be easily controlled by a reversible α/γ phase transformation with a remarkably high driving force of a few hundred MJ/m^3. The 9CrODS ferritic steel is recognized as a composite-like material composed of a residual ferrite and tempered martensite. The residual ferrite is a metastable phase, and high-temperature strength of 9CrODS steel is significantly ascribed to the presence of the metastable type of the residual ferrite. In this article, formation process of the composite-like structure and resultant superior high-temperature strength of the 9CrODS steel are reviewed with incorporating current result of manufacturing in terms of newly developed thermo-mechanical processing.

2. Formation of composite-like material

The composite-like structure of 9CrODS steel is controlled by the α/γ phase transformation of the steel, which yields the residual ferrite embedded in the tempered martensite. The nano-sized oxide particles are concomitantly distributed among both phases. This section describes the process governing a formation of composite-like structure.

2.1 Manufacturing process

Pure elemental powders of iron (99.5 mass%, 45 – 100 μm), carbon (99.7 mass%, 5 μm), chromium (99.9 mass%, under 250 μm), tungsten (99.9 mass%, 4.5 – 7.5 μm), and titanium (99.7 mass%, under 150 μm) were mechanically alloyed (MAed) together with Y_2O_3 powder (99.9 mass%, 20 nm) for 48 h in an argon gas atmosphere using a planetary-type ball mill (Fritsch P-6). Pots with a volume of 250cm^3 were rotated at a speed of 420 rpm; the pots contained the powders (35 g) and balls (total weight: 350 g); the weight ratio of the balls to the powders was set at 10:1. The standard chemical composition of MAed powders produced is Fe – 9Cr – 0.13C – 2W – 0.2Ti – 0.35Y_2O_3 (mass%). The excess oxygen (Ex.O) was measured to be 0.09 mass%, which was determined by subtracting the amount of oxygen

contained in Y_2O_3 from the total oxygen content; this amount of oxygen is inevitable for the formation of a Y – Ti complex oxide.

The MAed powders were consolidated by spark plasma sintering (SPS) or hot-isostatic-pressing (HIP) at 1,150 °C for 1 h. The final heat treatment was conducted by normazing at 1,050 °C for 1 h and tempered at 800 °C for 1 h. Microstructure of the produced 9CrODS steel is shown in Fig.1. The structure is of the dual-phase, composed of a smooth surface phase and surrounding tempered martensite containing black dots type of chromium carbide (Ukai, 2011). This smooth surface phase belongs to a residual ferrite, of which formation process is mentioned in the next section.

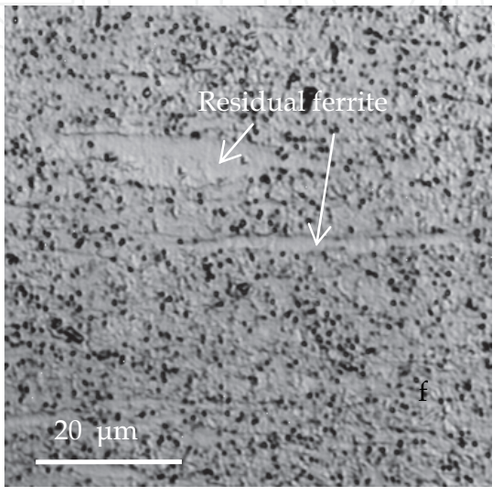

Fig. 1. Mirostructure of 9CrODS steel taken by laser-microscopy, showing a residual ferrite surrounded by the tempered martensite (Ukai, 2011).

2.2 Residual ferrite formation

The computed phase diagram of the Fe – 9Cr – 0.13C – 2W – 0.2Ti system without Y_2O_3 is shown in Fig. 2 (a) with respect to the carbon content (Yamamoto et al., 2011). For a nominal carbon content of 0.13 mass%, the single austenite γ-phase containing TiC carbide is stable at the normalizing temperature of 1050 °C. The equilibrium γ/γ+δ phase boundary at this temperature corresponds to a carbon content of 0.08 mass%, beyond which δ-ferrite is not stable. Fig. 3 shows SEM micrographs of the MAed powders for specimens with 0.1 mass%, 0.35 mass% and 0.7 mass% Y_2O_3 and without Y_2O_3 that were heat-treated by normalizing at 1050 °C and quenching in water (Yamamoto et al., 2010). The specimens without and with 0.1 mass% Y_2O_3 have the single martensite structure, which were obtained by inducing the transformation from the γ-phase by water quenching. This result is consistent with the computed phase diagram shown in Fig. 2(a). Nevertheless, the specimens with 0.35 mass% and 0.7 mass% Y_2O_3 exhibit a dual phase comprising martensite and smooth surface phases.

Digital image analyses showed that the area fraction of the smooth surface phase was approximately 0.2 for both specimens with 0.35 mass% and 0.7 mass% Y_2O_3. No obvious difference was observed between X-ray diffraction peaks of the martensite-phase and smooth surface phases at room temperature.However, high-temperature X-ray diffraction measurement at 950 °C showed a considerable difference, as shown in Fig. 4; the specimen without Y_2O_3 had diffraction peaks corresponding only to the austenite γ-phase, whereas specimens with 0.35 mass% and 0.7 mass% Y_2O_3 had diffraction peaks corresponding to the

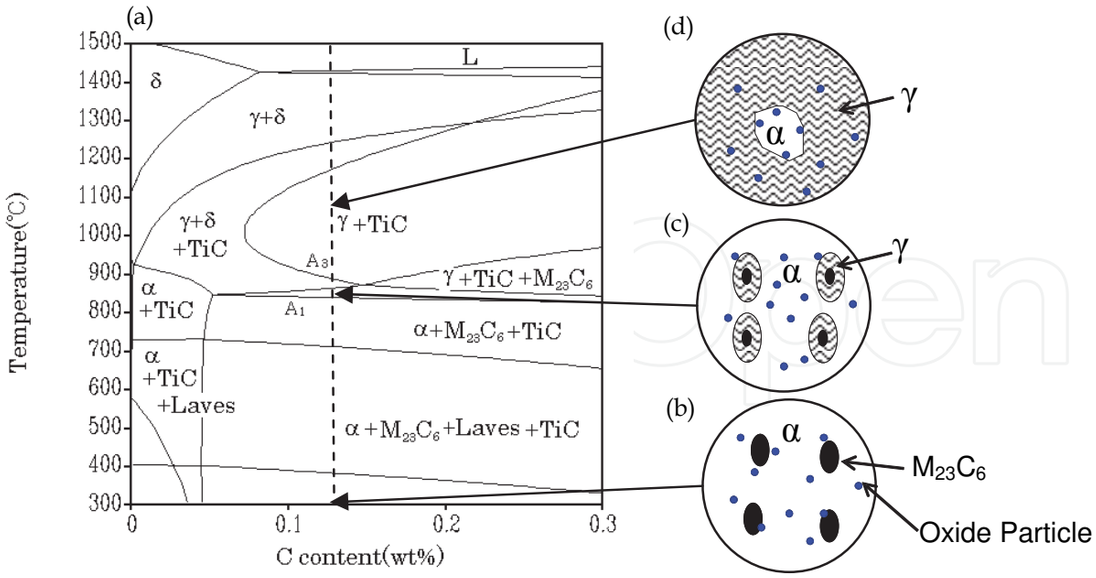

Fig. 2. (a) Computed phase diagram with respect to carbon content for Fe–9Cr–xC–0.2Ti–2W without oxide particle and schematic image at, (b) room temperature, (c) A_{C1} point, and (d) 1050 °C for system with oxide particle (Yamamoto et al., 2011).

austenite γ-phase and the ferrite phase (Yamamoto et al., 2010). The austenite γ-phase transformed to the martensite-phase, but the ferrite phase remained unchanged by water quenching. These results prove that the smooth surface phase is composed of ferrite. Considering that the ferrite phase is formed only in the specimens containing 0.35 mass% and 0.7 mass% Y_2O_3 and that four types of ODS steels shown in Fig. 3 have an identical chemical composition except for Y_2O_3 content, it seems that the presence of a Y_2O_3 particle favors the retention of the ferrite phase at 950 °C and 1050 °C.

Dilatometric measurement was also carried out from the room temperature to 1100 °C with a heating rate and a cooling rate of 5 °C/min. Fig. 5 shows the results of the dilatometric measurement when Fe – 9Cr – 0.13C – 2W – 0.2Ti was heated without and with 0.35 mass% Y_2O_3 (Yamamoto et al., 2010). In the case of the specimen without Y_2O_3, the linear thermal expansion coefficients started decreasing from A_{C1} point of 850 °C to A_{C3} point of 880 °C because of the reverse transformation of the martensite-phase to the γ-phase, which was in reasonably good agreement with the computed phase diagram shown in Fig. 2(a). The addition of 0.35 mass% Y_2O_3 induced an increase of up to the A_{C3} point of 930 °C. By comparing both the curves, we found that the specimen with 0.35 mass% Y_2O_3 exhibited a smaller amount of reduction in the linear thermal expansion during the reverse transformation of the martensite-phase to the γ-phase; this observation indicates that the entire martensite-phase was not transformed to the γ-phase. The untransformed ferrite phase corresponds to that observed by the X-ray diffraction peaks in the specimen with 0.35 mass% Y_2O_3 at 950 °C. This untransformed ferrite phase was designated as the residual ferrite. More detail consideration is discussed from a viewpoint of difference in the thermal expansion coefficient in reference (Yamamoto et al., 2010)

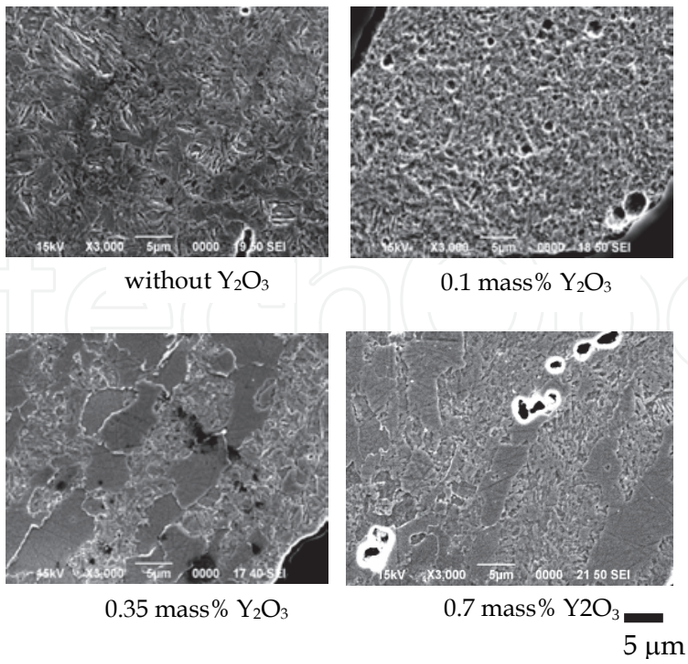

Fig. 3. SEM photographs of the MAed powders for 0 mass%, 0.1 mass%, 0.35 mass% and 0.7 mass% Y_2O_3 specimens after normalizing at 1050 °C and subsequently quenched to water (Yamamoto et al., 2010).

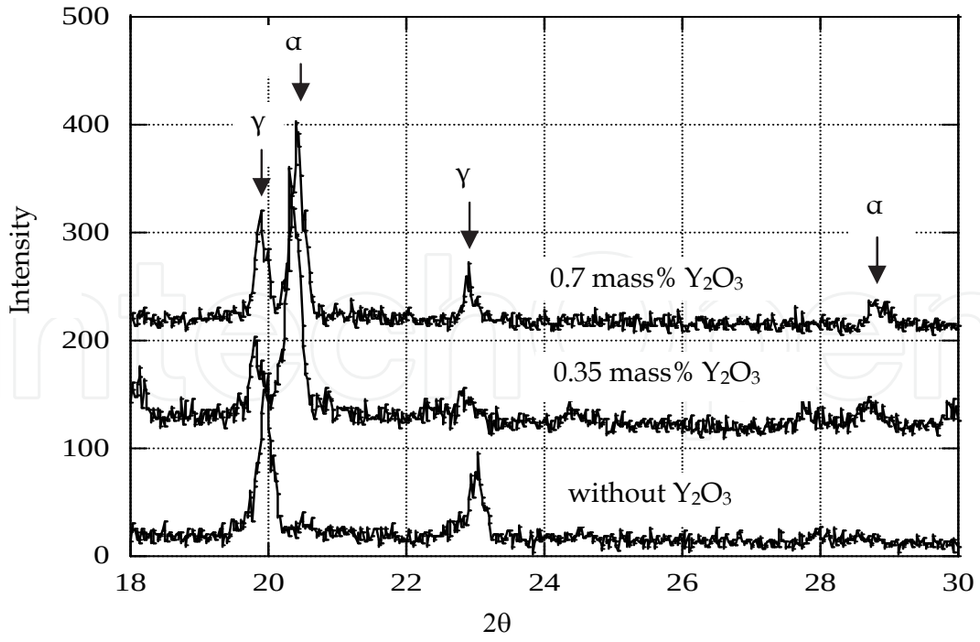

Fig. 4. Results of X-ray diffraction measurement at 950 °C for 0 mass%, 0.35 mass% ,and 0.7 mass% Y_2O_3 specimens (Yamamoto et al., 2010).

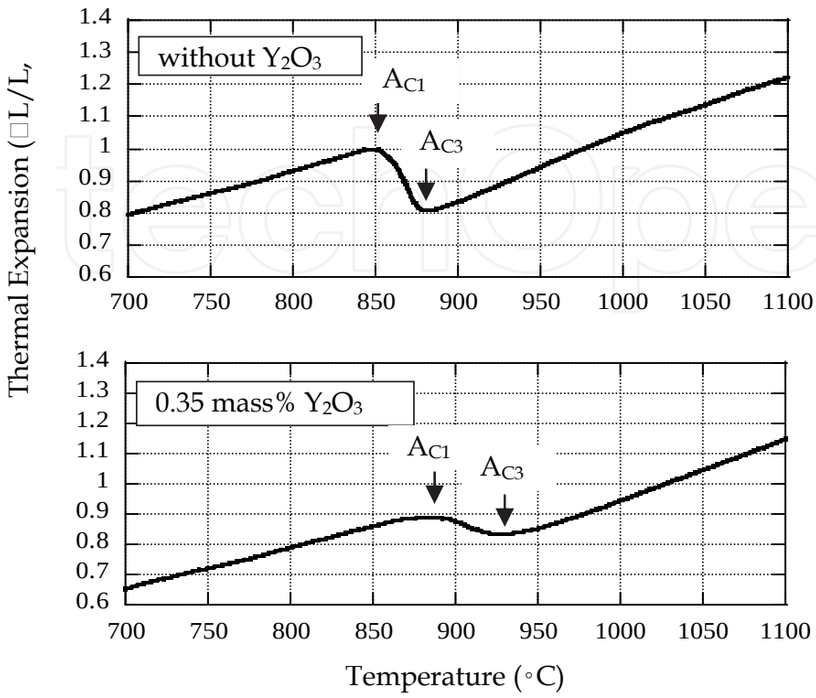

Fig. 5. Results of thermal expansion measurement between 700 °C and 1100 °C at temperature rising of 0.33 °C/s for 0 mass% and 0.35 mass% Y_2O_3 specimens (Yamamoto et al., 2010).

2.3 Thermodynamic analyses

Alinger et al. carried out a small angle neutron scattering (SANS) experiment for a U14YWT specimen (Fe – 14Cr – 0.4Ti – 3W – 0.25Y_2O_3). The neutron scattering cross-section and scattering vector were measured for the MAed powder after hot-isostatic-pressing (HIP) or thermal annealing at 700 °C, 850 °C, 1000 °C, and 1150 °C. Their results indicate that the MAed powder annealed at 700 °C shows the smallest radius and highest density for the Y – Ti complex oxide particles (Alinger et al., 2004). Assuming that the Y_2O_3 particles were decomposed during mechanical alloying, the subsequent annealing resulted in the formation and precipitation of Y – Ti complex oxide particles at elevated temperatures of 700 °C or higher. Since the reverse transformation of the ferrite α-phase to the austenite γ-phase took place at the elevated temperature of over 850 °C, which is higher than the precipitation temperature of the Y – Ti complex oxide particles, it is possible to consider that the partial retention of the residual ferrite can be attributed to the presence of the Y – Ti complex oxide particles in the 9CrODS ferritic steels; these particles should block the motion of the α/γ interface, thereby partly suppressing the reverse transformation of the α-phase to the γ-phase.

The chemical driving force (ΔG) for the reverse transformation of the α-phase to the γ-phase in the Fe – 0.13C – 2W – 0.2Ti system without Y_2O_3 can be evaluated in terms of Gibbs free energy vs. carbon content curves at each temperature; these curves were derived by using

the Thermo-Calc code and TCFE6 database. The pinning force (*F*) against the motion of α/γ interface can be expressed as equation (1), which was obtained from the modified Zener equation (Nishizawa et al., 1997).

$$F = \frac{3}{8}\frac{\sigma \cdot f_p^{2/3}}{r} \tag{1}$$

where σ (J/m²) is the interfacial energy between α and γ-phase and its value was selected to be 0.56 J/m² (Martion & Doherty, 1976). *r* (m) is the radius of the oxide particles in the α-phase. The chemical form of the oxide particles was determined to be $Y_2Ti_2O_7$ by TEM, and their diameter was estimated to be about 3 nm in the specimen of the same composition. Thus, r was set as 1.5 nm. f_p is the volume fraction of dispersed oxide particles, and it was derived on the basis of the experimental evidence that oxide particles consist of $Y_2Ti_2O_7$. The velocity of the α/γ interface motion (v) is proportional to the difference between F and ΔG, as shown in equation (2):

$$v = M \times (\Delta G - F) \tag{2}$$

M is the mobility of the interface. ΔG and *F* are competitive, and ΔG> F indicates a positive velocity for the interface motion, i.e., the reverse transformation of the α-phase to the γ-phase. On the other hand, ΔG< F indicated that the α/γ interface could be pinned by oxide particles, and thus the α-phase was retained.

When the chemical driving force (ΔG) for the reverse transformation of the α-phase to the γ-phase is derived, we should consider a change of carbon content in the matrix due to carbide dissolution, because carbon content greatly affects the Gibbs energy of γ-phase. At A_{C1} point, $M_{23}C_6$ carbide dissolves into matrix and carbon concentration at carbide-matrix interface becomes relatively high. For example, carbon content of 0.2 mass % leads to ΔG higher than pinning force F by oxide particle at 1050 °C as shown in Fig. 6 (Yamamoto et al.,

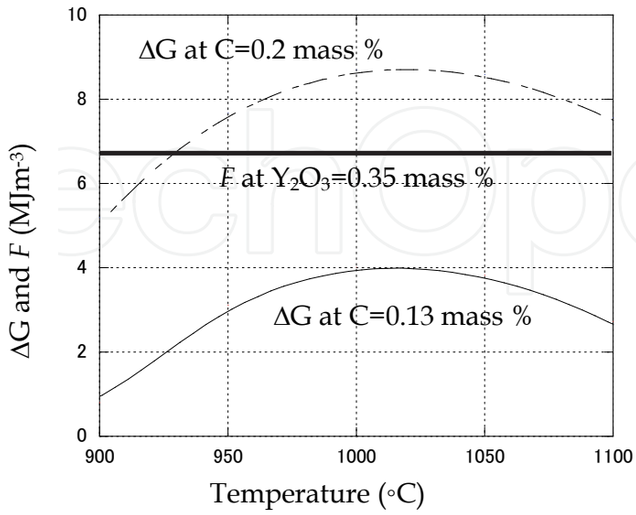

Fig. 6. Comparison of the driving force (ΔG) for α to γ reverse transformation and the pinning force (*F*) by oxide particle: C denotes carbon content (Yamamoto et al., 2011).

2011). This result suggests that α to γ reverse transformation proceeds from the carbide-matrix interface, where $M_{23}C_6$ carbide dissolves into matrix. This situation is schematically illustrated in Fig. 2(c). When temperature rises up beyond A_{C3} point, $M_{23}C_6$ carbide completely dissolves into matrix and thereby average carbon concentration approaches to the initial content of 0.13 mass %, where pinning force *F* is higher than driving force ΔG, as shown in Fig. 6. This result of calculation implies that α-ferrite can partially remain, as schematically shown in Fig. 2(d). Besides, on the basis of the above calculation, the formation and volume fraction of the residual ferrite is able to be controlled by appropriate amount of carbon in the matrix. We have successfully adjusted the volume fraction of the residual ferrite by controlling a direct addition of carbon or oxygen that affects the matrix carbon content through either TiO_2 or TiC formation (Ukai et al., 2007).

2.4 Oxide particle dispersion

The size distribution of oxide particles within the residual ferrite and the tempered martensite matrix was separately evaluated. In this study, both ODS fully ferritic steel and ODS fully martensitic steel were produced to simulate the residual ferrite and martensite phases, respectively, where the microstructure of the fully ferrite is completely the same as residual ferrite, because both phases are not transformed to γ-phase at the temperature above A_{C3} point. Fig. 7 shows the dispersed oxide particles in full martensite and full ferrite ODS steels, observed by TEM (Ukai, 2011). It is obvious that a few nm size oxide particles are finely dispersed in the fully ferrite ODS steel, whereas their size is coarser in the

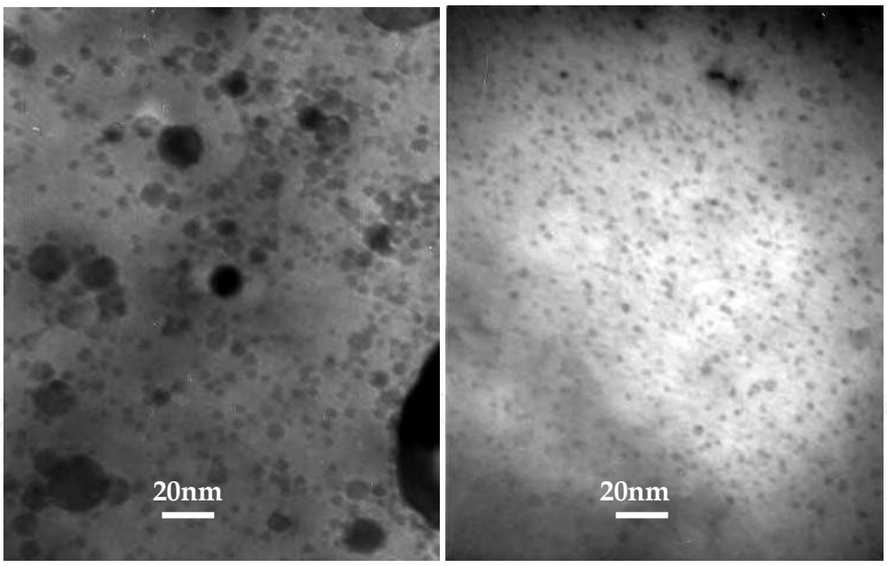

Fig. 7. TEM micrographs showing oxide particles in (a) ODS fully martensitic steel (b) ODS fully ferritic steel, residual ferrite (Ukai, 2011).

martensite ODS steel. The image analysis of the TEM micrographs is shown in Fig. 8; the mean size of oxide particle in full ferrite and full martensite ODS steels is 3 nm and 7 nm, respectively (yamamoto et al., 2011). From Fig. 8, the oxide particles dispersed in the ODS fully martensitic steel, i.e. martensite matrix, seems to shift to a coarser size compared to the dispersion in ODS fully ferritic steel, i.e. residual ferrite. One of the main reasons for this behavior could be associated with α/γ reverse transformation. Yazawa et al. reported that

the coherent to incoherent transition at precipitation interfaces sometimes induces coarsening of precipitates (Yazawa et al., 2004). Similar behavior is expected in the ODS martensite matrix. Our consideration is schematically shown in Fig.9. The oxide particles

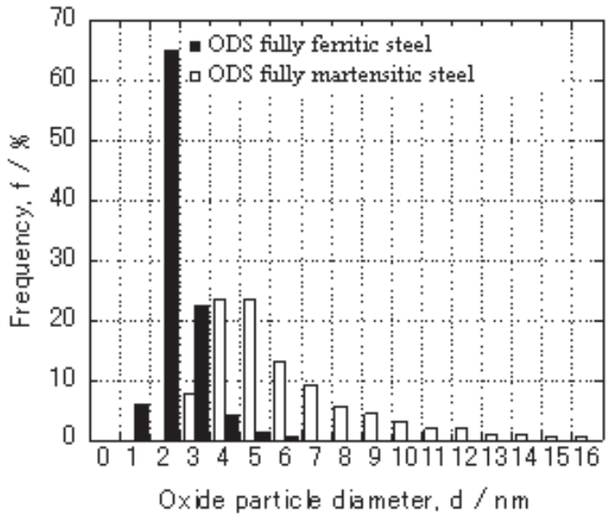

Fig. 8. Oxide particle size distributions in ODS fully ferritic steel and ODS fully martensitic steel (Yamamoto et al., 2011)

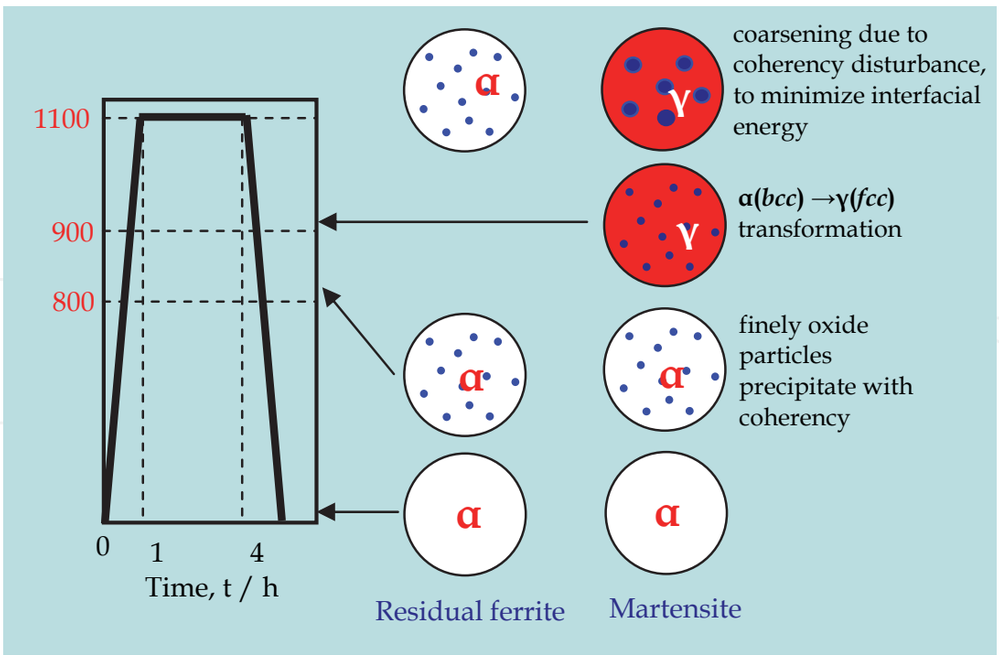

Fig. 9. Schematic representation of a process of the oxide particle coarsening in the martensite phase, compared to the residual ferrite with fine oxide particles by keeping coherency.

are formed by a process of precipitation during hot-pressing at 1100 °C after their decomposition was induced by mechanical alloying. This precipitation leads to partially coherency between oxide particles and the α-ferrite matrix, since precipitation takes place at temperatures below the A_{C1} point (Alinger et al., 2004). Subsequent change of the matrix phase from α-bcc crystal structure to γ-fcc by the reverse transformation could disturb the interfacial coherency; the oxide particles coarsen to minimize the interfacial energy during staying at γ-phase. Therefore, martensite phase transformed from γ-phase by cooling contains larger size of oxide particles, whist the residual ferrite contains finer oxide particles due to keeping coherency.

3. Creep deformation characterization

The creep deformation of the 9CrODS steel is unique and so different from that of the existed heat-resistant steels. The packet and block boundaries also play an important role for deformation. This section characterizes a deformation mechanism of the 9CrODS steel from a viewpoint of composite-like behavior.

3.1 Nano-hardness of residual ferrite

With the aim of evaluating the mechanical property of the residual ferrite, nanoindentation measurements were conducted using a Berkovich tip-type indentator at a loading of 3 mN. The trace of a Berkovich tip of sub-micron size can be placed within the interiors of the residual ferrite regions, while the conventional micro-Vickers diamond tips using 100 mN loads cover 7 x 7 micron-meters. Considering that the plastic zone is only two to three times larger than the contact area of the Berkovich tip, the mechanical property of the residual ferrite can be adequately evaluated by nanoindentaion measurements. Fig.10 shows the hardness change in the individual phases as a parameter of the tempering conditions (Ukai et al., 2009). The tempering parameters are shown in equation (3) in in terms of a Larson-Miller parameter (LMP; C = 20);

$$\mathrm{LMP} = \mathrm{T}\,(20 + \log \mathrm{t}) \tag{3}$$

where T is temperature in kelvin and t is time in hours. The time at different temperature can be derived so as to satisfy the same LMP value.. The hardness decrease is significantly restricted in the residual ferrite with increasing tempering conditions compared with that of the martensite phase. The overall hardness measured by the micro-Vickers tester is also shown by the broken line; this covers both the residual ferrite and martensite, thereby representing the average hardness of both phases. The hardness H_v is correlated with the yield stress σ_y using the following relationship (Tabor, 1951):

$$\sigma_y = 1/3\ H_v\ . \tag{4}$$

By tempering at 800 °C for 58 h, which is equivalent to tempering at 700 °C for 10,000 h based on the LMP, the hardness can be converted to the yield stress at room temperature for the individual phases: 1360 MPa for the residual ferrite and 930 MPa for the martensite. One of the main reasons for increasing hardness at the residual ferrite is come from the dispersion strengthening of oxide particles that are finely distributed in the residual ferrite as mentioned in the previous section. It is worth noting, therefore, that 9CrODS steel behaves like composite material comprising of hard and soft elements.

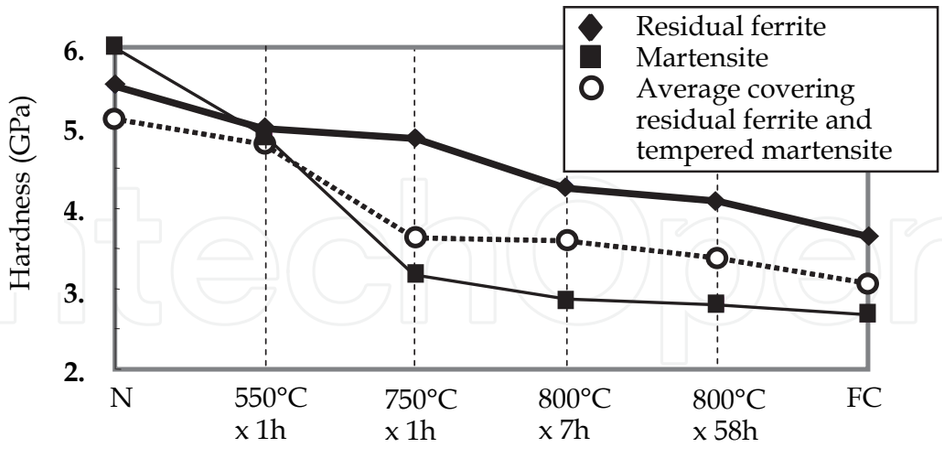

Fig. 10. Hardness change as a function of tempering conditions for the individual phases of residual ferrite and martensite measured by nanoindentator as well as average covering both measured by micro-Vickers; N: normalizing, FC: furnace cooling (Ukai et al., 2009).

3.2 Creep strain curve

Fig. 11 shows the typical creep curve of 9CrODS steel after normalizing and tempering (NT) for stress loadings of 155 MPa and 230 MPa at 700 °C (Ukai et al., 2009). The optical microstructure of this specimen is shown in the left upper of Fig. 12 (Ukai et al., 2009). This steel is composed of the residual ferrite and the tempered martensite. The secondary creep is obviously decelerated with strain accumulation, and the specimen ruptured without an accelerated creep region at 155 MPa. A stepwise increase in the primary creep strain can be observed with stress increase up to 230 MPa. These behaviors are completely different from those of conventional heat-resistant steels. In conventional steels, the rupture occurs after the accelerated creep deformation, where coarsening of carbides, movement of the lath and block boundaries and a local recovery of dislocations become dominant (Abe, 2004, 2008).

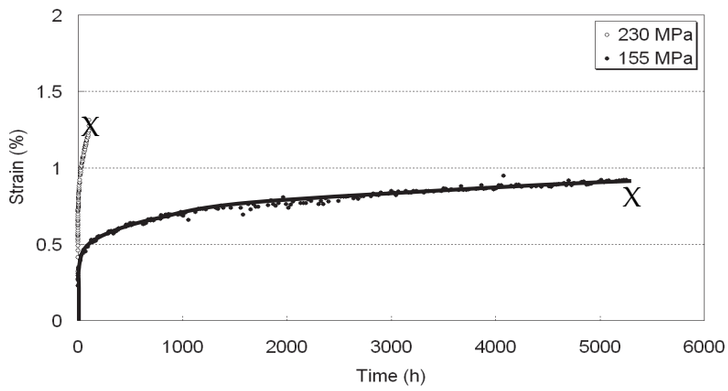

Fig. 11. Creep strain curves of 9CrODS steel after NT in the stress loading of 155 MPa and 230 MPa at 700 °C (Ukai et al.,2009).

Such dynamic recovery and structure coarsening should be suppressed by the dispersed nano-size oxide particles in 9CrODS steel. Their dominant fracture mode could be deformation near block and packet boundaries. The stress induced by this deformation can't be easily relaxed by the dislocation creep, since nano-size oxide particles can block the dislocation movement. This is the reason why the creep strain rate gradually decreases with increasing strain, and work hardening dominantly occurs during creep deformation.

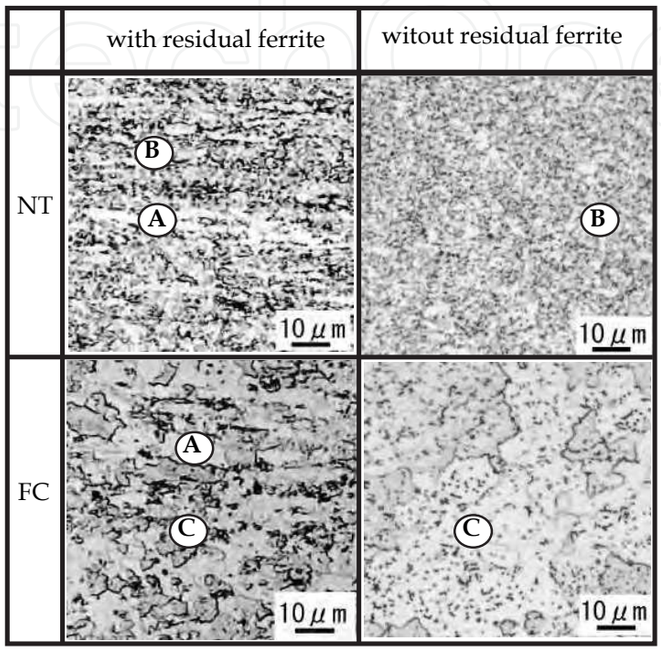

Fig. 12. Optical micrographs of 9CrODS steels with and without residual ferrite in the heat treatment conditions of normalizing and tempering (NT) and furnace cooling (FC). A: residual ferrite, B: tempered martensite, C: transformed ferrite (Ukai et al.,2009).

3.3 Creep rupture property

The optical microstructures of 9CrODS steels with and without the residual ferrite are shown in Fig. 12 for NT and furnace cooling (FC) conditions. The 9CrODS steel containing the residual ferrite has a standard chemical composition, whilst higher content of excess oxygen was added for the free residual ferrite one, where the titanium combines with oxygen rather than carbon, thus increase of matrix carbon content leads to complete α to γ transformation. The detail is mention in reference (Ukai & Ohtsuka, 2007). Based on the continuous cooling transformation (CCT) diagram, NT treatment induces the tempered martensite due to a rapid cooling rate of 7000 °C /h, while FC treatment causes a diffusional transformation to the α-phase by slow cooling at a rate of 30 °C /h.

Fig.13 shows their creep rupture strength (Ukai et al.,2009). The following two characteristic features were observed in creep rupture properties of 9CrODS steels. The first is that the creep rupture strength of NT with residual ferrite (TM+RF) increases stepwise from that of NT without residual ferrite (TM). This is attributed to the effects of the harder residual ferrite strengthening the 9Cr-ODS steels, therefore. The second feature is that the furnace cooling (FC) heat treatment for with or without residual ferrite induces stepwise increases in the creep rupture strength in comparison with the NT heat treatment. This result means that

the α-phase has superior strength to that of martensite. Martensitic phase transformation produces the packet and block boundaries, where grain boundary deformation and fracture can be preferably originated. The strength improvement in the α-phase induced by FC could be, therefore, due to the suppression of the deformation at packet and block boundaries.

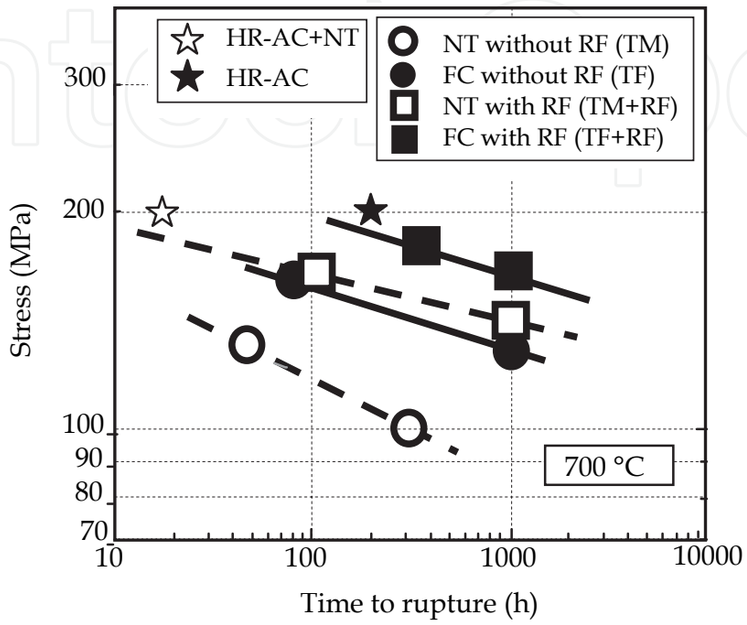

HR: hot-rolling
NT: normalizing and tempering
FC: furnace cooling
TM: tempered martensite
TF: transformed ferrite
TM+RF: tempered martensite and residual ferrite
TF+RF: transformed ferrite and residual ferrite

Fig. 13. Creep rupture data of 9CrODS steels with and without residual ferrite after NT and FC; creep rupture data of HR-AC and HR-AC-NT are also superimposed at 700 °C (Ukai et al.,2009).

3.4 Creep strain rate vs. stress relation

The threshold stress for deformation at 700 °C is estimated on the basis of equation (5) (Scattergood & Bacon, 1975).

$$\sigma = \frac{AMGb}{2\pi\lambda}\left[\ln\frac{D}{r_0} + B\right], \tag{5}$$

where, G is the shear modulus (50.6 GPa at 700 °C); M, the Taylor factor (3.0) (Stoller & Zinkle, 2000); b, the magnitude of the Burgers vector (2.48×10^{-10} m). The parameter r_o is the inner cut-off radius of a dislocation core, which was assumed to be the magnitude of the Burgers vector. In addition, λ is the average face-to-face distance between particles on a slip

plane; it is given in terms of the average particle radius r_s and the average center-to-center distance l_s between the particles :

$$\lambda = 1.25\, l_s - 2r_s \tag{6}$$

The values of l_s and r_s are determined using the particle radius r:

$$l_s = \sqrt{2\pi \overline{r^3}} / \sqrt{3f\bar{r}} \tag{7}$$

$$r_s = \pi / 4 \cdot (\overline{r^2} / \bar{r}) \tag{8}$$

where f is the volume fraction of the dispersed particles, which is estimated from the oxide particle density (4.84×10^3 Kg/m^3). The D corresponds to harmonic mean of $2r_s$ and λ. At the elevated temperature of 700 °C, the interface between the particles and matrix could tend to slide. Under such condition, an attractive interaction between a dislocation and the particles can be applied, as proposed by Srolovitz (Srolovitz et al., 1983). The A and B values are expressed by following formula.

$$A = \left[1 - \frac{\nu}{1-\nu}\sin^2\phi\right]\cos\phi, \quad B = 0.7 \qquad \text{for edge dislocation (9)}$$

$$A = \left[\frac{1+\nu\sin^2\phi}{1-\nu}\right]\cos\phi, \quad B = 0.6 \qquad \text{for screw dislocation (10)}$$

where ϕ is the critical angle at which the dislocation detaches from the particles: φ = 46° for a screw dislocation and ϕ = 19° for an edge dislocation. ν is the Poisson's ratio (0.334). Substituting these dispersion parameters into equation (5), the threshold stress σ for the average of edge and screw dislocations is derived to be 265 MPa. Fig. 14 shows the strain rate vs. stress relation (Ukai et al., 2009). The deformation occurs at a stress far below the threshold stress of 265 MPa. The deformation is, therefore, induced at weaker regions such as grain boundaries rather than being intra-grain themselves, which is strengthened by the dispersed oxide particles. The strain rate vs. stress relation is almost parallel, and the slope corresponding to a stress exponent n is estimated to be ranging from 10 to 14. It is well known that the typical value of the stress exponent is significantly higher (around 40) for deformation that is dominated by particle-dislocation interaction (Arzt, 1991). Therefore, the accelerated deformation at a lower stress level could have arisen from the local deformation associated with packet and block boundaries. The cause of this stress increase at which creep strain initiates by furnace cooling can be explained by a disappearance of packet and block boundaries, as described above. The residual ferrite also enlarges the critical stress for initiating creep strain. Concerning this phenomenon, the creep constitutive equation of 9CrODS steel should be formulated by analogy with a fiber composite material (Sakasegawa et al., 2008). From the stress distribution between the hardened residual ferrite and the softened tempered martensite, the stress loading on the tempered martensite is derived by the following equation:

$$\sigma_m / \sigma_t = 1/\{1 + (D - 1)\, f_r\}, \tag{11}$$

where σ_t and σ_m are the total stress loading and stress onto the individual tempered martensite regions, respectively. The parameter f_r is the volume fraction of the residual ferrite grains, and D is the stress distribution coefficient expressed as a ratio of the shear modulus of residual ferrite μ_r to that of the tempered martensite μ_m:

$$D = \mu_r/\mu_m. \tag{12}$$

Assuming that the shear modulus ratio is approximately expressed as the hardness ratio of both phases, D becomes equal to 1.46 from Fig.10. Thus, based on Equation (12), σ_m/σ_t is equal to 0.88 using f_r = 0.3, as determined by microstructure observation. This estimation implies that the stress loading onto the softened tempered martensite decreases to 0.88, which leads to increase in the stress corresponding to the initiation of creep strain.

As a summary of the creep deformation of 9CrODS steel, Fig. 15 schematically illustrates a configuration of the hardened residual ferrite and softened tempered martensite. Under stress loading, softened tempered martensite is preferentially deformed. Dislocations piled up at the packet and block boundaries could induce the localized deformation near these boundaries, since the intra-grain deformation is hardly taken place due to finely dispersed nano-sized oxide particles. The stress accumulated at such boundaries could lead to fracture. The hardened residual ferrite provides not only sharing the stress loading onto the softened tempered martensite, but also geometrically restricting the deformation of the softened tempered martensite. It can be said that deformation and fracture of the 9CrODS steel behaves like composite material.

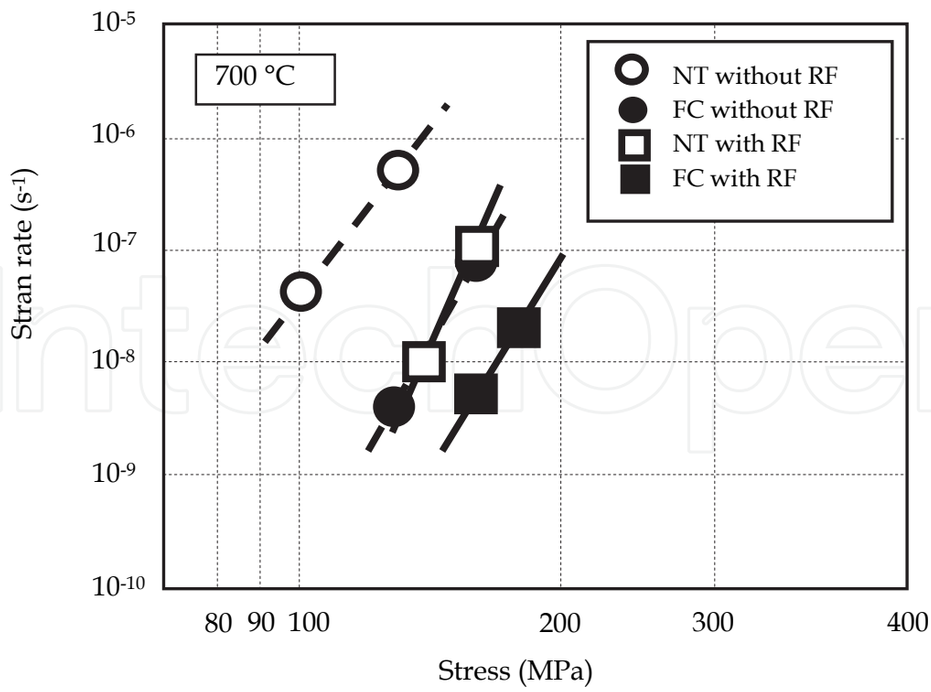

Fig. 14. Strain rate vs. stress relationship for 9CrODS steels with and without residual ferrite after NT and FC heat treatment (Ukai et al., 2009).

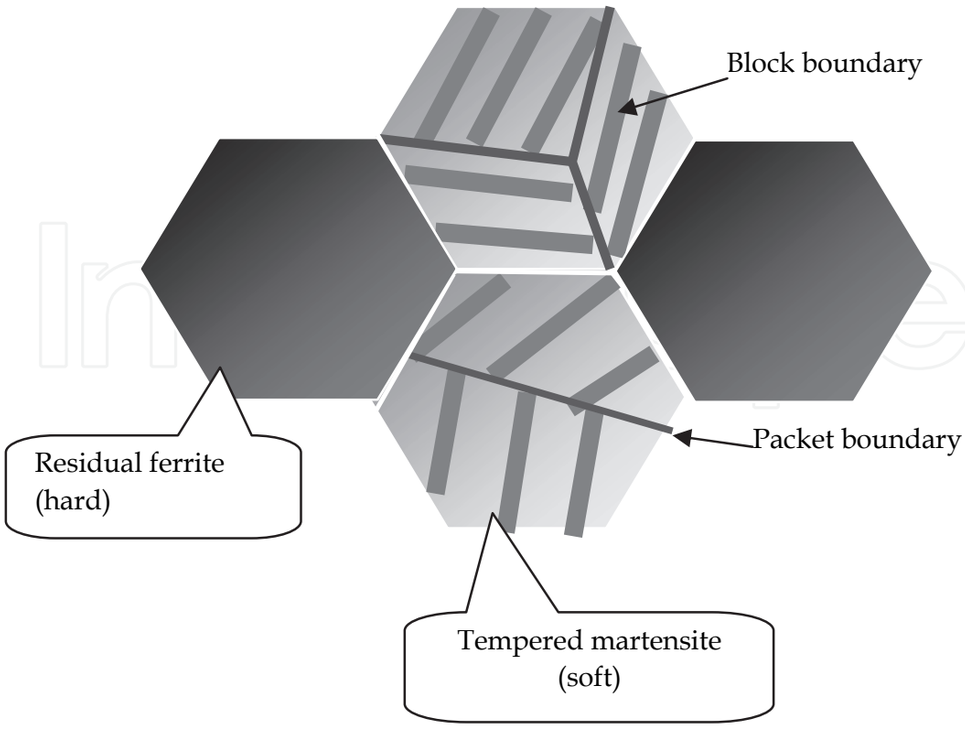

Fig. 15. Illustration of the hardened residual ferrite and softened tempered martensite.

4. Thermo-mechanical processing

Modification of a microstructure is required for the tempered martensite in 9CrODS steel, to suppress the localized deformation at packet and block boundaries. Hot-rolling was recently processed for this purpose. The results of currently developed thermo-mechanical processing and resultant high-temperature strength are assessed in this section.

4.1 Microstructure

The 9CrODS steel powders in the standard composition and high carbon content (0.41 mass%) were mechanically alloyed by the planetarium type boll mill, where high carbon specimen was prepared to produce the free residual ferrite 9CrODS steel. MAed powders were consolidated by spark plasma sintering (SPS) at 1100 °C and 44 MPa for 1 h; the hot-rolling (HRing) was conducted in the total reduction rate of 84 % at the austenitic γ phase region. The detail condition is as follow;

1. keeping temperature at 1,100 °C for 1 min in the furnace and taking out from the furnace.
2. hot-rolling at three times in the total reduction ratio of 52 %; temperature decreases to 930 °C
3. back to furnace to keep temperature at 1,100°C for 10 min and taking out from the furnace
4. again hot-rolling at three times in the total reduction ratio of 67 %; temperature decreases to 840°C at the end of hot-rolling, and air-cooled (AC) to room temperature in the cooling rate of 4000 °C/h.

As a parameter, normalizing (N) by water quench and tempering (T) heat-treatments were subsequently carried out at 1050 °C × 1 h and 800 °C × 1 h, respectively, to evaluate structure change of the HRed specimens.

Fig. 16 shows SEM micrographs of high carbon specimen (0.41mass%): (a) HR-AC and (b) subsequent NT heat treatment. Both structures are significantly different and the coarsened grains are formed just after HR-AC, whilst subsequent NT heat treatment induces finely homogeneous and the typical tempered martensite that is usual structure of 9CrODS steel without residual ferrite similar to the right upper optical photo of Fig. 12. The larger grains in HR-AC belong to ferrite that was transformed from the γ-phase during the air cooling after HR. A surrounding area is martensite structure. The microstructure of the standard 9CrODS steel is shown in Fig. 17. The larger grains are also observed in HR-AC specimen, and subsequent NT one has fine grains that involve the residual ferrite and tempered martensite similar to the left upper photo of Fig. 12. The coarsened grains in HR-AC specimen shown in Fig. 17(a) could be composed of the residual ferrite and transformed ferrite, however, it is difficult to separate them by SEM photograph, since both are the same ferrite phases.

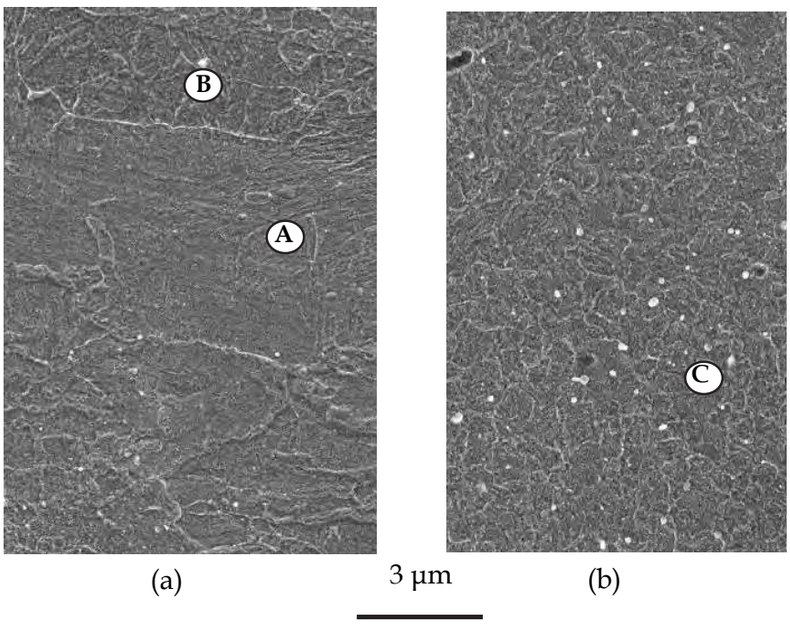

Fig. 16. SEM micrographs of 0.41 mass% carbon 9CrODS steel: (a) hot-rolling and air-cooling (HR-AC), (b) HR-AC and normalizing and tempering (NT); A: transformed ferrite, B: martensite, C: tempered martensite

Concerning a formation of the coarsened ferrite grains, it is obvious that these grains do not correspond to the coarsened residual ferrite, since coarsened grains are seen even in high carbon specimen without the residual ferrite as shown in Fig. 16(a). It is considered that the finer γ-grains made by hot rolling at 1000 °C accelerate the ferrite formation rather than martensite transformation during air cooling, from a viewpoint of a continuous cooling transformation (CCT) diagram of 9CrODS steels (Ukai & Ohtsuka, 2007). Furthermore, accumulation of severe strain energy in γ-grains induced by hot-rolling could be responsible for coarsening of the transformed ferrite grains.

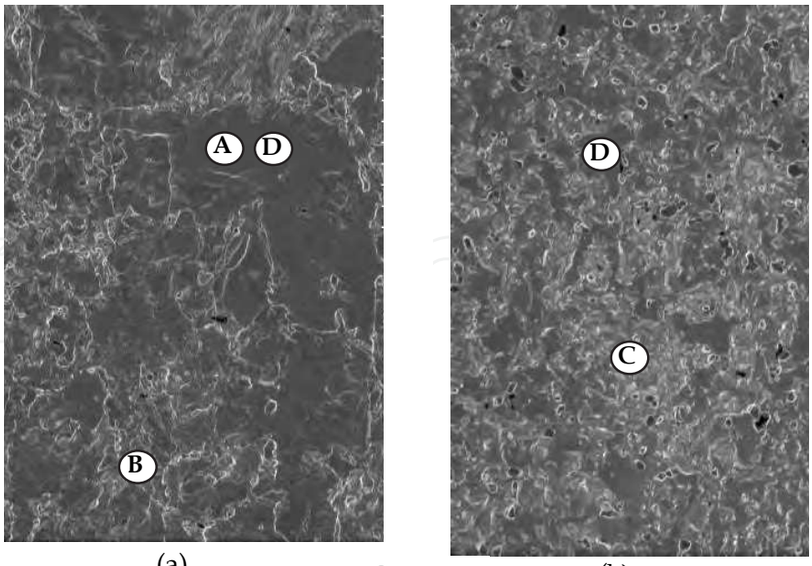

Fig. 17. SEM micrographs of standard 9CrODS steel: (a) hot-rolling and air-cooling (HR-AC), (b) HR-AC and normalizing and tempering (NT); A: transformed ferrite, B: martensite, C: tempered martensite, D: residual ferrite

4.2 High-temperature mechanical properties

The results of the tensile test at 700 °C are shown in Fig. 18. This test was conducted for the standard 9CrODS steel, varying with just HR-AC and subsequent NT heat treatment. The NT specimen exhibits the same level of strength and ductility as the conventional 9Cr-ODS steels [6]. This result can be understood by considering that the structure induced by HR completely disappears by normalizing heat treatment and its structure is composed of the residual ferrite and tempered marutensite as shown in Fig. 17(b). For HR-AC condition, the tensile strength and rupture elongation are recorded more than 500 MPa and 20 %, respectively. It is to be noticed that these tensile properties are adequately improved by HR-AC treatment far beyond those of the conventional 9CrODS steels.The excellent tensile performance of HR-AC specimen is ascribed to an existing of the transformed ferrite grains in the coarser size, which is shown in Fig. 17(a). The block and packet boundaries in martensite structure sometimes give appropriate sites for fracture, and thus lead to premature rupture (Abe, 2004). The coarsened ferritic grains could suppress the grain boundary deformation, and thus improve the tensile strength and ductility.

The creep rupture data of the standard 9CrODS steel for HR-AC and subsequent NT specimens were superimposed by star symbols in Fig. 13, where data are shown in the stress-rupture time correlation at 700 °C. The creep rupture strength of HR-AC specimen (solid star symbol) obtained in this test at 700 °C and 200 MPa approximately lies on the extrapolated line of FC specimen, but it is slightly higher. This improved strength over FC could be owing to the coarsening of the ferrite grains made by hot-rolling. Subsequent NT specimen also shows slightly higher strength than NT condition of the previous specimen containing the residual ferrite. Based on those finding, it is to be noticed that the ferrite grains in coarser size adequately improve the creep strength. This is due to a suppression of the block and packet boundary deformation, as mentioned in the tensile test.

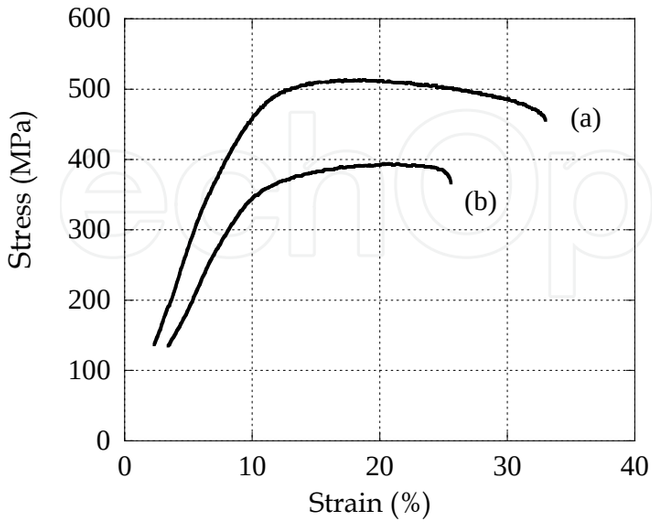

Fig. 18. The results of tensile tests of standard 9CrODS steel: (a) hot-rolling and air-cooling (HR-AC), (b) HR-AC and normalizing and tempering (NT).

5. Conclusion

The 9CrODS steel is an attractive composite-like material consisted of the residual ferrite and tempered martensite. Formation of both phases can be controlled by the process of α-γ phase transformation. The residual ferrite is a metastable phase and involves extremely finer nano-size oxide particles that are responsible for harder hardness; on the contrary, the tempered martensite contains coarser oxide particles and thus being softer hardness. Mechanical response of 9CrODS steel is completely different from that of the existed heat-resistant steels. Under stress loading, softened tempered martensite is preferentially deformed, in particular at the packet and block boundaries. The stress accumulation could give rise to a localized fracture along the packet and block boundaries in the tempered martensite. The microstructure of the tempered martensite was modified in terms of thermo-mechanical processing, and high-temperature strength was significantly improved through changing microstructure from the martensite to the transformed ferrite. The hardened residual ferrite plays a key role that provides a geometrical restriction for the deformation of softened tempered martensite. The best microstructure of 9CrODS steel is considered to be composed of hardened residual ferrite and softened transformed ferrite with free block and packet boundaries.

6. Acknowledgment

The author wishes to acknowledge many colleagues: in particular Mr. Takeji Kaito and Dr. Satoshi Ohtsuka of Japan Atomic Energy Agency (JAEA) and Dr. Takanari Okuda of Kobelco Research Institute Co. and Dr. Tsukasa Azuma of Japan Steel Works (JSW). The author would like to also thank many graduate students of my laboratory.

7. References

Abe, F. (2004). Bainitic and Martensitic Creep-Resistant Steels. *Curr. Opin. Sol. State Mater. Sci*. 8, 305 – 311

Abe, F. (2008). *Creep-Resistance Steels*, Edited by F. Abe, T-Ulf Kern and R. Viswanathan, The Institute of Materials, Minerals & Mining

Alinger,M. J., Oddett, G.R. & Hoelzer, D.T. (2004). The Development and Stability of Y–Ti–O anoclusters in Mechanically Alloyed Fe–Cr Based Ferritic Alloys. *J. Nucl. Mater.* 329 – 333, pp.382 – 386

Arzt, E. (1991). Creep of Dispersion Strengthened Materials: A Critical Assessment. *Res. Mech.* 31, pp.399 – 453

Martion, J.W. & Doherty, R.D. (1976). *Stability of Microstructure in Metallic Systems*, Cambridge University Press, Cambridge, pp. 173.

Nishizawa, T., Ohnuma, I. & Ishida, K. (1997). Examination of the Zener Relationship between Grain Size and Particle Dispersion. *Mater. Trans*. 38, 11, pp.950 – 956.

Odette, G.R., Alinger, M.J. & Wirth, B.D. (2008). Recent Developments in Irradiation-Resistant Steels. *Annu. Rev. Mater. Res*. 38, pp.471 – 503

Ohtsuka, S., Ukai, S., Fujiwara, M., Kaito, T. & Narita, T. (2004). Improvement of 9Cr-ODS Martensitic Steel Properties by Controlling Excess Oxygen and Titanium Contents. *J. Nucl. Mater*. 329 – 333, pp.372 – 376

Ohtuska, S., Ukai, S., Fujiwara, M., Kaito, T. & Narita, T. (2005a). Improvement of Mechanical Properties of 9CrODS Martensitic Steel by Controlling Titanium Concentration. *Mater. Trans*. 46, 3, pp.487 – 492

Ohtsuka, S., Ukai, S., Fujiwara, M., Kaito, T. & Narita, T. (2005b). Nano-structure Control in ODS Martensitic Steels by Means of Selecting Titanium and Oxygen Contents. *J. Phys. Chem. Solids*. 66, pp.571 – 575

Ohtsuka, S., Ukai, S. & Fujiwara, M. (2006). Nano-Mesoscopic Structural Control in 9CrODS Ferritic/Martensitic Steels. *J. Nucl. Mater*. 351, pp.241 – 246

Ohtsuka, S., Ukai, S., Fujiwara, M., Sakasegawa, H., Kaito, T. & Narita, T. (2007). Nano-Mesoscopic Structural Characterization of 9Cr-ODS Martensitic Steel for Improving Creep Strength. *J. Nucl. Mater*. 367 – 370, pp.160 – 165

Sakasegawa, H., Ukai a, S., Tamura, M., Ohtsuka, S., Tanigawa, H., Ogiwara, H., Kohyama, A. & Fujiwara, M. (2008). Creep Constitutive Equation of Dual Phase 9Cr-ODS Steel. *J. Nucl. Mater*. 373, pp.82 – 89

Scattergood, R.O. & Bacon, D.J. (1975). The Orowan Mechanism in Anisotropic Crystals. *Phil. Mag*. A 31, pp.179 – 198

Srolovitz, D.J., Petkovic-Luton, R.A & Luton, M.J. (1983). Edge Dislocation-Circular Inclusion Interactions at Elevated Temperatures. Acta Metall. 31, pp.2151 – 2159

Stoller, R.E & Zinkle, S.J. (2000). On the Relationship between Uniaxial Yield Strength and Resolved Shear Stress in Polycrystalline Materials. *J. Nucl. Mater.* 283 – 287, pp.349 – 352

Tabor, D. (1951). *The Hardness of Metals*, Oxford University Press, Oxford

Ukai, S., Nishida, T., Okuda, T. & Yoshitake, T. (1998). R&D of Oxide Dispersion Strengthened Ferritic/Martensitic Steels for FBR. *J. Nucl. Mater*. 258–263, pp.1745–1749

Ukai, S. & Fujiwara, M. (2002a). Perspective of ODS Alloys Application in Nucrlear Environment. *J. Nucl. Mate*r. 307–311, pp.749–757

Ukai, S., Mizuta, S., Fujiwara, M., Okuda, T. & Kobayashi, T. (2002b). Consolidation Process Study of 9Cr-ODS Martensitic Steel Tubes. *J. Nucl. Mater*. 307–311, pp.758–76

Ukai, S., Kaito, T., Otsuka, S., Narita, T., Fujiwara, M. & Kobayashi, T. (2003). Production and Properties of Nano-Scale 9Cr-ODS Martensitic Steel Claddings. *ISIJ Int*. 43, 12, pp.2038–2045

Ukai, S. & Ohtsuka, S. (2007). Nano-mesoscopic Structure Control in 9Cr-ODS Ferritic Steels. *Energy Mater*. 2, 1, pp.26 – 35

Ukai, S., Ohtsuka, S., Kaito, T., Sakasegawa, H., Chikata, N. & Hayashi, S. (2009). High-Temperature Strength Characterization of Advanced 9Cr-ODS Ferritic Steels. *Materials Science and Engineering.* A 510-511, pp.115-120

Ukai, S. (2011). Oxide Dispersion Strengthened Steels. *Comprehensive Nuclear Materials*. Elsevier, in press

Yamamoto, M., Ukai, S., Hayashi, S., Kaito, T. & Ohtsuka, S. (2010). Formation of Residual Ferrite in 9Cr-ODS Ferritic Steels. *Materials Science and Engineering* A 527, pp.4418 – 4423

Yamamoto, M., Ukai, S., Hayashi, S., Kaito, T. & Ohtsuka, S. (2011). Reverse Phase Transformation from α to γ in 9Cr-ODS Ferritic Steels. J. Nucl. Mater., in press

Yazawa, Y., Furuhara, T. & Maki, T. (2004). Effect of Matrix Recrystallization on Morphology, Crystallography and Coarsening Behavior of Vanadium Carbide in Austenite. *Acta Metall*. 52, pp.3727 – 3736

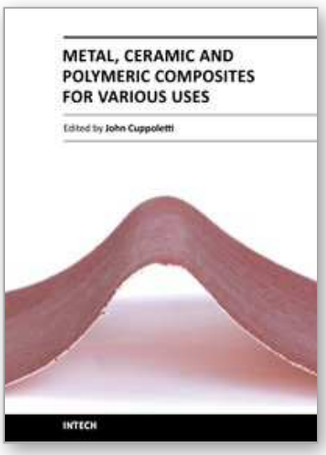

Metal, Ceramic and Polymeric Composites for Various Uses
Edited by Dr. John Cuppoletti

ISBN 978-953-307-353-8
Hard cover, 684 pages
Publisher InTech
Published online 20, July, 2011
Published in print edition July, 2011

Composite materials, often shortened to composites, are engineered or naturally occurring materials made from two or more constituent materials with significantly different physical or chemical properties which remain separate and distinct at the macroscopic or microscopic scale within the finished structure. The aim of this book is to provide comprehensive reference and text on composite materials and structures. This book will cover aspects of design, production, manufacturing, exploitation and maintenance of composite materials. The scope of the book covers scientific, technological and practical concepts concerning research, development and realization of composites.

How to reference
In order to correctly reference this scholarly work, feel free to copy and paste the following:

Shigeharu Ukai (2011). Microstructure and High-Temperature Strength of 9CrODS Ferritic Steel, Metal, Ceramic and Polymeric Composites for Various Uses, Dr. John Cuppoletti (Ed.), ISBN: 978-953-307-353-8, InTech, Available from: http://www.intechopen.com/books/metal-ceramic-and-polymeric-composites-for-various-uses/microstructure-and-high-temperature-strength-of-9crods-ferritic-steel

INTECH
open science | open minds

InTech Europe
University Campus STeP Ri
Slavka Krautzeka 83/A
51000 Rijeka, Croatia
Phone: +385 (51) 770 447
Fax: +385 (51) 686 166
www.intechopen.com

InTech China
Unit 405, Office Block, Hotel Equatorial Shanghai
No.65, Yan An Road (West), Shanghai, 200040, China
中国上海市延安西路65号上海国际贵都大饭店办公楼405单元
Phone: +86-21-62489820
Fax: +86-21-62489821

IntechOpen